

Second Order Statistics of Non-Isotropic UAV Ricean Fading Channels

(Invited Paper)

Linzhou Zeng¹, Xiang Cheng¹, Cheng-Xiang Wang², and Xuefeng Yin³

¹State Key Laboratory of Advanced Optical Communication Systems and Networks,
School of Electronics Engineering and Computer Science, Peking University, Beijing, 100871, China

²Institute of Sensors, Signals and Systems,
School of Engineering and Physical Sciences, Heriot-Watt University, Edinburgh, EH14 4AS, UK

³College of Electronics and Information Engineering, Tongji University, Shanghai, 201804, China

Email: {linzhou.zeng, xiangcheng}@pku.edu.cn, cheng-xiang.wang@hw.ac.uk, yinxuefeng@tongji.edu.cn

Abstract—A three-dimensional (3D) theoretical model for unmanned aerial vehicle (UAV) communications is proposed in this paper. From the theoretical model, the envelope level crossing rate (LCR) and average fade duration (AFD) are derived under a 3D propagation environment. Based on the derived expressions, we for the first time investigate the LCR and AFD for UAV channels with different UAV-related parameters. The close agreement between the theoretical results and measured data demonstrates the utility of the proposed model.

I. INTRODUCTION

UAV communications have become a hot topic in advancing 5G networks, since it can provide a wide-range coverage for connection [1]-[3]. The UAV-aided communication systems have both the transmitter and receiver in motion with significantly different elevations, and the high mobility and moving direction of UAVs are significant and unique factors to the communication performance. For the system design, it is necessary to have a detailed understanding of the UAV fading channel and its statistical properties.

For now, some research groups have conducted measurement campaigns [4]-[11] and worked on developing generic channel models [12]-[20] to characterize UAV channels. In [19] and [20], UAV channel measurements and modeling has been comprehensively investigated in detail and demonstrated some useful and interesting conclusions. These UAV channel models can be broadly categorized as deterministic models and stochastic models. The deterministic models, using the ray-tracing method or the finite difference time domain (FDTD) method, were proposed in [12] and [14]. The stochastic models can be further classified as non-geometrical stochastic models (NGSMs) and geometry-based stochastic models (GBSMs). For NGSMs, the most classical one is the statistical model [15]-[16], which is essentially an stochastic process, e.g., Gaussian or Ricean process. The curved-earth two-ray (CE2R) model has been proposed [17]-[20] for high-altitude (or long-distance) UAV communication scenarios, where the ground curvature cannot be neglected, and the received signal mainly consists of a line-of-sight (LoS) component and a surface reflection. Unlike NGSMs, GBSMs utilize simplified ray-tracing rules on the effective scatterers that are randomly dis-

tributed in a geometrical shape to mimic multipath channels. Since GBSM directly deals with scatterers, it can naturally model fast time-variant characteristics of channels by properly mimicking the property of scatterers. Therefore, the GBSM approach has been widely used for modeling vehicle-to-vehicle (V2V) channels [21]-[24]. Recently, the GBSM approach has been used for UAV channel modeling. In [25], a 3D cylinder GBSM had been developed for UAV channels. While, a 3D sphere GBSM had been proposed for UAV channels in [26].

The aforementioned papers mainly focused on the study of first-order statistics and space-time correlation properties. To assess communication-system characteristics, such as handoff, velocities of the transmitter and receiver, and fading rate, it is of great importance to study the second-order statistics derived from channel models. The envelope level crossing rate (LCR) and average fade duration (AFD) are two important ones that characterize the temporal fluctuations of received envelope. To derive the LCR and AFD, we first propose a generic 3D geometry-based stochastic model that employs a two-cylinder model and obtains the complex faded envelope as a superposition of the line-of-sight (LoS), single-bounced, and double-bounced rays. From the theoretical model, we derive the LCR and AFD for a 3D non-isotropic scattering environment and investigate the impact of important model parameters on them. Finally, we compare the analytical results for the LCR and AFD with the measured data in [15]. Excellent agreement between them demonstrates the utility of the proposed model.

The remainder of this paper is organized as follows. Section II presents a 3D theoretical model to derive the LCR and AFD. Section III derives the LCR and AFD of the complex envelope for 3D non-isotropic scattering environments. Section IV compares analytical and measurement results to verify theoretical derivations. Finally, Section V provides some conclusions.

II. A THEORETICAL MODEL FOR UAV CHANNELS

Let us now consider a narrowband single-user UAV communication system. Both the Tx and Rx are in motion and equipped with single antenna. The propagation scenario is

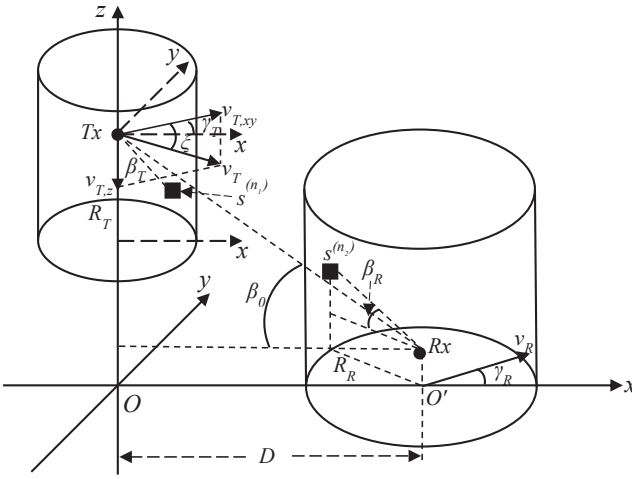


Fig. 1. A generic channel model with LoS components, single- and double-bounced rays for UAV channels.

characterized by a non-isotropic scattering with possibly a LoS component between the Tx and Rx.

Fig. 1 illustrates the geometry of the proposed two-cylinder GBSM. The proposed model has two cylinders to place effective scatterers, one around the Tx and the other around the Rx. We suppose there are N_1 effective scatterers around the Tx lying on the surface of a cylinder of radius R_T , and the n_1 th ($n_1 = 1, 2, \dots, N_1$) effective scatterer is denoted by $s^{(n_1)}$. Similarly, suppose there are N_2 effective scatterers around the Rx lying on the surface of a cylinder of radius R_R , and the n_2 th ($n_2 = 1, 2, \dots, N_2$) effective scatterer is denoted by $s^{(n_2)}$. The horizontal and vertical distance between the Tx and Rx is D and H , respectively. We assume the Tx and Rx move with speeds of v_T and v_R , respectively. As shown in Fig. 1, we decompose the vector v_T into a horizontal component $v_{T,xy}$ and a perpendicular component $v_{T,z}$, and then define $\langle v_{T,xy}, v_T \rangle = \xi$, and $\langle v_{T,xy}, +x \rangle = \gamma_T$, where $\langle \cdot, \cdot \rangle$ denotes the included angle. This angle pair, ξ and γ_T , is used to characterize the UAV movement in a 3D space. For the Rx, namely the ground user, it moves in the direction of γ_R in the xy plane. The AoA of the wave traveling from an effective scatterer $s^{(n_i)}$ ($i = 1, 2$) toward the Rx is denoted by $\beta_R^{(n_i)}$, and the AoD of the wave that impinges on the effective scatterer $s^{(n_i)}$ is designated by $\beta_T^{(n_i)}$. The AoD and AoA of the LoS path are α_T^{LoS} , β_T^{LoS} , α_R^{LoS} , and β_R^{LoS} , respectively.

The received complex fading envelope between the Tx (T) and the Rx (R) at the carrier frequency f_c is a superposition of the LoS single-bounced, and double-bounced components.

$$h_{TR}(t) = h_{TR}^{LoS}(t) + h_{TR}^{SBT}(t) + h_{TR}^{SBR}(t) + h_{TR}^{DB}(t) \quad (1)$$

where

$$\begin{aligned} h_{TR}^{LoS}(t) &= \sqrt{\frac{K\Omega_{TR}}{K+1}} e^{-j2\pi f_c \tau_{TR}} \\ &\quad e^{j2\pi f_{Tm} t [\cos(\alpha_T^{LoS}) - \gamma_T] \beta_T^{LoS} \cos \xi + \sin \beta_T^{LoS} \sin \xi}] \quad (2) \\ &\quad e^{j2\pi f_{Rm} t [\cos(\alpha_R^{LoS}) - \gamma_R] \cos \beta_R^{LoS}} \end{aligned}$$

$$\begin{aligned} h_{TR}^{SBT}(t) &= \sqrt{\frac{\eta_{SBT}\Omega_{TR}}{K+1}} \lim_{N_1 \rightarrow \infty} \frac{1}{\sqrt{N_1}} \sum_{n_1=1}^{N_1} e^{j\phi^{(n_1)}} e^{-2\pi f_c \tau_{pq,n_1}} \\ &\quad e^{j2\pi f_{Tm} t [\cos(\alpha_T^{(n_1)}) - \gamma_T] \cos \beta_T^{(n_1)} \cos \xi + \sin \beta_T^{(n_1)} \sin \xi]} \\ &\quad e^{j2\pi f_{Rm} t [\cos(\alpha_R^{(n_1)}) - \gamma_R] \cos \beta_R^{(n_1)}} \end{aligned} \quad (3)$$

$$\begin{aligned} h_{TR}^{SBR}(t) &= \sqrt{\frac{\eta_{SBR}\Omega_{TR}}{K+1}} \lim_{N_2 \rightarrow \infty} \frac{1}{\sqrt{N_2}} \sum_{n_2=1}^{N_2} e^{j\phi^{(n_2)}} e^{-2\pi f_c \tau_{pq,n_2}} \\ &\quad e^{j2\pi f_{Tm} t [\cos(\alpha_T^{(n_2)}) - \gamma_T] \cos \beta_T^{(n_2)} \cos \xi + \sin \beta_T^{(n_2)} \sin \xi]} \\ &\quad e^{j2\pi f_{Rm} t [\cos(\alpha_R^{(n_2)}) - \gamma_R] \cos \beta_R^{(n_2)}} \end{aligned} \quad (4)$$

$$\begin{aligned} h_{TR}^{DB}(t) &= \sqrt{\frac{\eta_{DB}\Omega_{TR}}{K+1}} \lim_{N_1, N_2 \rightarrow \infty} \frac{1}{\sqrt{N_1 N_2}} \sum_{n_1, n_2=1}^{N_1, N_2} e^{j\phi^{(n_1, n_2)}} e^{-2\pi f_c \tau_{pq,n_1, n_2}} \\ &\quad e^{j2\pi f_{Tm} t [\cos(\alpha_T^{(n_1)}) - \gamma_T] \cos \beta_T^{(n_1)} \cos \xi + \sin \beta_T^{(n_1)} \sin \xi]} \\ &\quad e^{j2\pi f_{Rm} t [\cos(\alpha_R^{(n_2)}) - \gamma_R] \cos \beta_R^{(n_2)}} \end{aligned} \quad (5)$$

In (2)-(5), $\tau_{TR} = \varepsilon_{TR}/c$, $\tau_{TR,n_1} = (\varepsilon_{Tn_1} + \varepsilon_{n_1 R})/c$, $\tau_{TR,n_2} = (\varepsilon_{n_2} + \varepsilon_{n_2 R})/c$, $\tau_{TR,n_1, n_2} = (\varepsilon_{Tn_1} + \varepsilon_{n_1 n_2} + \varepsilon_{n_2 R})/c$ are the waves' travel times through the link $T-R$, $T-s^{(n_1)}-R$, $T-s^{(n_2)}-R$, $T-s^{(n_1)}-s^{(n_2)}-R$, respectively, where c is the speed of light. The symbols K_{TR} and Ω_{TR} denote the Ricean K-factor and the total power of the $T-R$ link, respectively. Besides, η_{SBT} and η_{SBR} designate the contribution of the single- and double-bounced rays to the total scattered power $\Omega_{TR}/(K+1)$. Note that these energy-related parameters satisfy $\eta_{SBT} + \eta_{SBR} + \eta_{DB} = 1$. The scattering-caused phases $\phi^{(n_1)}$, $\phi^{(n_2)}$ and $\phi^{(n_1, n_2)}$ are independent and identically distributed (i.i.d) random variables with uniform distributions over $[-\pi, \pi]$. The maximum frequencies related to the movement of Tx and Rx are denoted by f_{Tm} and f_{Rm} , respectively.

From Fig. 1, we know that the AoD and AoA are independent for double-bounced rays, while they are geometrically interdependent for single-bounced rays. Below is the relationship of the AoD and AoA in single-bounce rays.

A. For SBT rays

$$\cos \alpha_R^{(n_1)} \approx -1 \quad (6)$$

$$\sin \alpha_R^{(n_1)} \approx \frac{\frac{R_T}{D} \sin \alpha_T^{(n_1)}}{1 - \frac{R_T}{D} \cos \alpha_T^{(n_1)}} \quad (7)$$

$$\begin{aligned} \cos \beta_R^{(n_1)} &\approx \cos \beta_0 + \frac{R_T}{D} \sin \beta_0 \cos \beta_0 \\ &\quad \cdot (\tan \beta_T^{(n_1)} \cos \beta_0 - \cos \alpha_T^{(n_1)} \sin \beta_0) \end{aligned} \quad (8)$$

$$\begin{aligned} \sin \beta_R^{(n_1)} &\approx \sin \beta_0 - \frac{R_T}{D} \cos^2 \beta_0 \\ &\quad \cdot (\tan \beta_T^{(n_1)} \cos \beta_0 - \cos \alpha_T^{(n_1)} \sin \beta_0). \end{aligned} \quad (9)$$

B. For SBR rays

$$\cos \alpha_T^{(n_2)} \approx 1 \quad (10)$$

$$\sin \alpha_T^{(n_2)} \approx \frac{\frac{R_R}{D} \sin \alpha_R^{(n_2)}}{1 + \frac{R_R}{D} \cos \alpha_R^{(n_2)}} \quad (11)$$

$$\begin{aligned} \cos \beta_T^{(n_2)} &\approx \cos \beta_0 + \frac{R_R}{D} \sin \beta_0 \cos \beta_0 \\ &\cdot (\tan \beta_R^{(n_2)} \cos \beta_0 + \cos \alpha_R^{(n_2)} \sin \beta_0) \end{aligned} \quad (12)$$

$$\begin{aligned} \sin \beta_T^{(n_2)} &\approx \sin \beta_0 - \frac{R_R}{D} \cos^2 \beta_0 \\ &\cdot (\tan \beta_R^{(n_2)} \cos \beta_0 + \cos \alpha_R^{(n_2)} \sin \beta_0). \end{aligned} \quad (13)$$

Since the number of effective scatterers is assumed to be infinite, i.e., $N_1, N_2 \rightarrow \infty$, our model is actually a mathematical reference model, which cannot be implemented in practice due to the infinite complexity. However, a reference model is useful for theoretical analysis of wireless channels, and is also a starting point for a realizable simulation model. For our reference model, the discrete expressions of the AoA and AoD, i.e., $\alpha_R^{(n_i)}$, $\beta_R^{(n_i)}$ and $\alpha_T^{(n_i)}$, $\beta_T^{(n_i)}$, can be replaced by continuous expressions α_R , β_R and α_T , β_T . Besides, we assume the random variables α_T , β_T , α_R , and β_R are independent. Therefore, the joint PDF of these angles can be written as the product of marginal PDFs of the AoA and AoD. In this paper, we use the von Mises PDF to characterize the azimuth angles α_T and α_R . The von-Mises PDF is defined as

$$f(\alpha) = \frac{e^{k \cos(\alpha - \alpha_\mu)}}{2\pi I_0(k)}, -\pi \leq \alpha \leq \pi \quad (14)$$

where $I_0(\cdot)$ is the zeroth-order modified Bessel function of the first kind, and $\alpha_\mu \in [-\pi, \pi]$ is the mean angle at which the scatterers are distributed in the xy plane. The parameter k controls the spread around the mean angle, and increasing k incurs more non-isotropic scattering. The elevation angles β_T and β_R is described as the cosine PDF, which is defined as

$$f(\beta) = \frac{\pi}{4\beta_m} \cos\left(\frac{\pi}{2} \frac{\beta - \beta_\mu}{\beta_m}\right), |\beta - \beta_\mu| \leq \beta_m \leq \frac{\pi}{2}. \quad (15)$$

Note that $\beta \in [\beta_\mu - \beta_m, \beta_\mu + \beta_m]$. For simplicity, we let $\beta_\mu - \beta_m = \beta_1$ and $\beta_\mu + \beta_m = \beta_2$, i.e., $\beta \in [\beta_1, \beta_2]$. Applying these PDFs to the AoA and AoD, we have

$$f(\alpha_T) = \frac{e^{k_T \cos(\alpha_T - \alpha_{T\mu})}}{2\pi I_0(k_T)}, -\pi \leq \alpha_T \leq \pi \quad (16)$$

$$f(\alpha_R) = \frac{e^{k_R \cos(\alpha_R - \alpha_{R\mu})}}{2\pi I_0(k_R)}, -\pi \leq \alpha_R \leq \pi \quad (17)$$

$$f(\beta_T) = \frac{\pi}{4\beta_{Tm}} \cos\left(\frac{\pi}{2} \frac{\beta_T - \beta_{T\mu}}{\beta_{Tm}}\right), \beta_{T1} \leq \beta_T \leq \beta_{T2} \quad (18)$$

$$f(\beta_R) = \frac{\pi}{4\beta_{Rm}} \cos\left(\frac{\pi}{2} \frac{\beta_R - \beta_{R\mu}}{\beta_{Rm}}\right), \beta_{R1} \leq \beta_R \leq \beta_{R2} \quad (19)$$

where $\beta_{T1} = \beta_{T\mu} - \beta_{Tm}$, $\beta_{T2} = \beta_{T\mu} + \beta_{Tm}$, $\beta_{R1} = \beta_{R\mu} - \beta_{Rm}$, and $\beta_{R2} = \beta_{R\mu} + \beta_{Rm}$.

The LCR at a specified level r , $L(r)$, is defined as the rate at which the signal envelope crosses level r in the positive/negative going direction. For Ricean fading channels, we can derive the expression of the LCR as

$$\begin{aligned} L(r) &= \frac{2r\sqrt{K+1}}{\pi^{\frac{3}{2}}} \sqrt{\frac{b_2}{b_0} - \frac{b_1^2}{b_0^2}} \cdot e^{-K-(K+1)r^2} \\ &\int_0^{\pi/2} \cosh(2\sqrt{K(K+1)r} \cos \theta) \cdot \\ &[e^{-(\chi \sin \theta)^2} + \sqrt{\pi} \chi \sin \theta \cdot \text{erf}(\chi \sin \theta)] d\theta \end{aligned} \quad (20)$$

where $\cosh(\cdot)$ is the hyperbolic cosine function, $\text{erf}(\cdot)$ is the error function, and $\chi = \sqrt{\frac{Kb_1^2}{b_0 b_2 - b_1^2}}$. Finally, parameters b_0 , b_1 , and b_2 are defined as

$$b_0 = \mathbb{E}[h_{TR}^I(t)^2] = \mathbb{E}[h_{TR}^Q(t)^2] \quad (21)$$

$$b_1 = \mathbb{E}[h_{TR}^I(t) h_{TR}^Q(t)] = \mathbb{E}[h_{TR}^Q(t) h_{TR}^I(t)] \quad (22)$$

$$b_2 = \mathbb{E}[\dot{h}_{TR}^I(t)^2] = \mathbb{E}[\dot{h}_{TR}^Q(t)^2] \quad (23)$$

where $h_{TR}^I(t)$ and $h_{TR}^Q(t)$ are the in-phase and quadrature components of the complex fading envelope $h_{TR}(t)$, and $\dot{h}_{TR}^I(t)$, $\dot{h}_{TR}^Q(t)$ are the first derivative of $h_{TR}^I(t)$ and $h_{TR}^Q(t)$, respectively.

By substituting (1) to (21)-(23), the parameters b_m ($m \in \{0, 1, 2\}$) becomes

$$b_m = b_m^{SBT} + b_m^{SBR} + b_m^{DB} \quad (24)$$

where

$$\begin{aligned} b_m^{SBT} &= \frac{\eta_{SBT}}{2(K+1)} (2\pi)^m \int_{\beta_{T1}}^{\beta_{T2}} \int_{-\pi}^{\pi} f(\alpha_T) f(\beta_T) \\ &\{f_{Tm}[\cos(\alpha_T - \gamma_T) \cos \beta_T \cos \xi + \sin \beta_T \sin \xi] \\ &+ f_{Rm}[\cos(\alpha_R - \gamma_R) \cos \beta_R]\}^m d\alpha_T d\beta_T \end{aligned} \quad (25)$$

$$\begin{aligned} b_m^{SBR} &= \frac{\eta_{SBR}}{2(K+1)} (2\pi)^m \int_{\beta_{R1}}^{\beta_{R2}} \int_{-\pi}^{\pi} f(\alpha_R) f(\beta_R) \\ &\{f_{Tm}[\cos(\alpha_T - \gamma_T) \cos \beta_T \cos \xi + \sin \beta_T \sin \xi] \\ &+ f_{Rm}[\cos(\alpha_R - \gamma_R) \cos \beta_R]\}^m d\alpha_R d\beta_R \end{aligned} \quad (26)$$

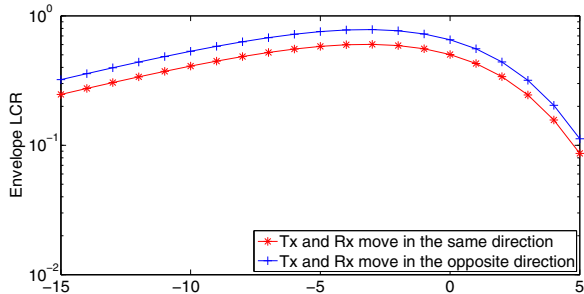
$$\begin{aligned} b_m^{DB} &= \frac{\eta_{DB}}{2(K+1)} (2\pi)^m \int_{\beta_{R1}}^{\beta_{R2}} \int_{-\pi}^{\pi} \int_{\beta_{T1}}^{\beta_{T2}} \int_{-\pi}^{\pi} f(\alpha_T) f(\beta_T) f(\alpha_R) f(\beta_R) \\ &\{f_{Tm}[\cos(\alpha_T - \gamma_T) \cos \beta_T \cos \xi + \sin \beta_T \sin \xi] \\ &+ f_{Rm}[\cos(\alpha_R - \gamma_R) \cos \beta_R]\}^m d\alpha_T d\beta_T d\alpha_R d\beta_R. \end{aligned} \quad (27)$$

Note that for $m = 0$, we have

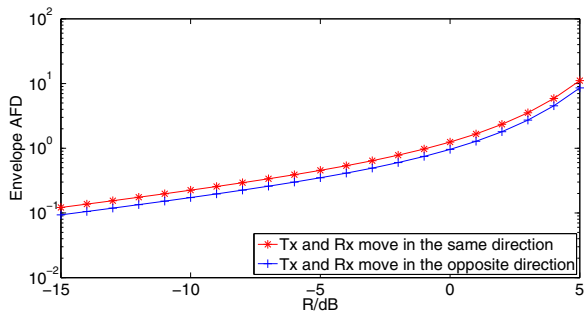
$$b_0 = b_0^{SBT} + b_0^{SBR} + b_0^{DB} = \frac{1}{2(K+1)} \quad (28)$$

where

$$\begin{aligned} b_0^{SBT} &= \frac{\eta_{SBT}}{2(K+1)} \int_{\beta_{T1}}^{\beta_{T2}} \int_{-\pi}^{\pi} f(\alpha_T) f(\beta_T) d\alpha_T d\beta_T \\ &= \frac{\eta_{SBT}}{2(K+1)} \end{aligned} \quad (29)$$



(a)



(b)

Fig. 2. Envelope LCR and AFD for different moving directions of the Tx and Rx.

$$b_0^{SBR} = \frac{\eta_{SBR}}{2(K+1)} \int_{\beta_{R1}}^{\beta_{R2}} \int_{-\pi}^{\pi} f(\alpha_R) f(\beta_R) d\alpha_R d\beta_R \quad (30)$$

$$= \frac{\eta_{SBR}}{2(K+1)}$$

$$b_0^{DB} = \frac{\eta_{DB}}{2(K+1)} \int_{\beta_{R1}}^{\beta_{R2}} \int_{-\pi}^{\pi} \int_{\beta_{T1}}^{\beta_{T2}} \int_{-\pi}^{\pi} f(\alpha_T) f(\beta_T) f(\alpha_R) f(\beta_R) d\alpha_T d\beta_T d\alpha_R d\beta_R \quad (31)$$

$$= \frac{\eta_{DB}}{2(K+1)}.$$

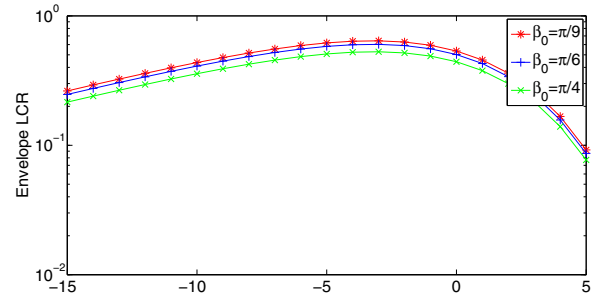
The AFD, $T(r)$, is defined as the average time over which the signal envelope, $|h_{TR}(t)|$, remains below a certain level r . In the proposed model, the AFD can be written as

$$T(r) = \frac{1 - Q(\sqrt{2K}, \sqrt{2(K+1)r^2})}{L(r)} \quad (32)$$

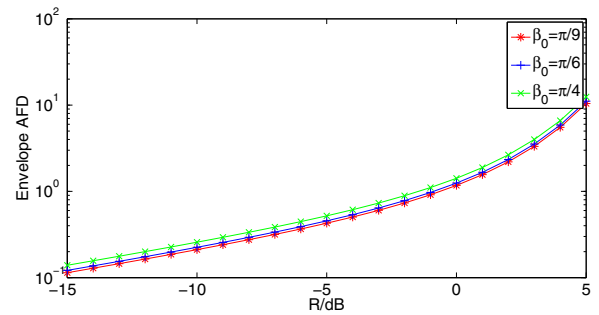
where $Q(\cdot)$ is the Marcum Q function. For NLoS conditions, the AFD in (32) simplifies to $T(r) = (1 - e^{-r^2})/L(r)$ by setting $K = 0$.

III. NUMERICAL RESULTS AND ANALYSIS

In this section, we investigate the derived LCR and AFD and compare the numerical results with the measured data in . The following parameters are used for our analysis: $D = 100m$, $H = 50m$, $\beta_0 = \pi/6$, $R_T = 5m$, $R_R = 3m$, $\lambda = 0.1m$, $v_T = 10m/s$, $v_R = 2m/s$, $\gamma_T = \gamma_R = 0$, $\xi = 0$, $\beta_{T\mu} = 0$, $\alpha_{T\mu} = 0$, $\beta_{R\mu} = \pi/4$, $\alpha_{R\mu} = \pi$, $k_T = 10$, $k_R = 3$, $\beta_{Tm} = \pi/6$, $\beta_{Rm} = \pi/6$, and $\theta_T = \theta_R = \pi/2$.



(a)



(b)

Fig. 3. Envelope LCR and AFD for different elevation angles of the UAV.

Fig. 2 shows the LCR and AFD for different moving directions of the Tx and Rx. It can be observed from Fig. 2 that the LCR is higher when Tx and Rx move in the opposite direction than the one when Tx and Rx move in the same direction.

Fig. 3 illustrates the impact of elevation angles of the UAV (i.e., the UAV's altitudes) on the envelope LCR and AFD. The power-related parameters are $K = 0.3$, $\eta_{SBR} = 0.1$, $\eta_{SBR} = 0.7$, $\eta_{DB} = 0.2$. It can be observed from Fig. 3 that the larger the β_0 , the lower the LCR, and the higher the AFD. It is because that increasing β_0 increases the distance between the UAV and the ground user, i.e., $D/\cos\beta_0$. The larger the distance $d(T, R)$, the smaller the impact of UAV movement, and thus the higher the temporal stability of UAV channels.

Fig. 4 compares the theoretical LCR/AFD with some measurement data, also from [15]. In Fig. 4, the environment-related parameters are $K = 0.03$, $\eta_{SBR} = 0.05$, $\eta_{SBR} = 0.9$, $\eta_{DB} = 0.05$, $\beta_0 = \pi/10$, $R_T = 20m$, $R_R = 105m$, $D = 1000m$, $k_T = 1$, $k_R = 0.5$. We have considered the measured path gain [15] when obtaining the theoretical LCR/AFD. As shown in Fig. 4, the excellent agreement between the theoretical results and the measurement data confirms the utility of the proposed model.

IV. CONCLUSIONS

In this paper, we have proposed a 3D two-cylinder GBSM for UAV Ricean channels and investigated the impact of some unique UAV-related parameters on the derived LCR and AFD. The good agreement between the theoretical results and the measured data has validated the utility of the proposed model.

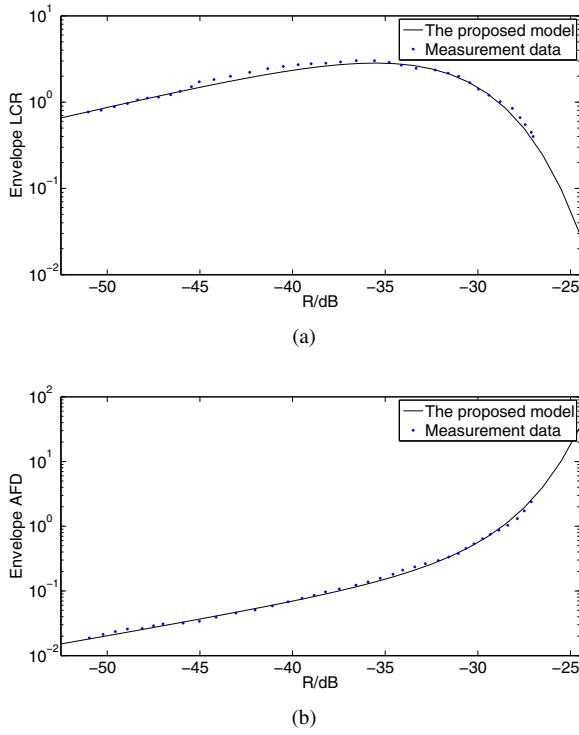


Fig. 4. Comparisons between the theoretical LCR/AFD and the measurement data.

V. ACKNOWLEDGMENT

This work was jointly supported by the National Natural Science Foundation of China (Grant No. 61622101, 61571020, and 61471268), Ministry National Key Research and Development Project under Grant 2016YFE0123100, the 863 Project in 5G (Grant No. 2014AA01A701), EU H2020 ITN 5G Wireless project (Grant No. 641985), EU FP7 QUICK project (Grant No. PIRSES-GA-2013-612652), and EPSRC TOUCAN project (Grant No. EP/L020009/1).

REFERENCES

- [1] Y. Zeng, R. Zhang, and T. J. Lim, "Wireless communications with unmanned aerial vehicles: opportunities and challenges," *IEEE Commun. Mag.*, vol. 54, no. 5, pp. 36–42, May 2016.
- [2] D. W. Matolak, "Unmanned aerial vehicles: Communications challenges and future aerial networking," in *Proc. ICNC*, Anaheim, CA, USA, Feb. 2015, pp. 567–572.
- [3] D. W. Matolak, "Air-ground channels & models: Comprehensive review and considerations for unmanned aircraft systems," in *Proc. IEEE Aerospace Conf.*, Big Sky, MT, USA, Mar. 2012, pp. 1–17.
- [4] J. Romeu, A. Aguasca, J. Alonso, S. Blanch, and R. R. Martins, "Small uav radiocommunication channel characterization," in *Proc. EuCAP*, Barcelona, Spain, Apr. 2010, pp. 1–5.
- [5] H. T. Kung, C. K. Lin, T. H. Lin, S. J. Tarsa, and D. Vlah, "Measuring diversity on a low-altitude uav in a ground-to-air wireless 802.11 mesh network," in *Proc. IEEE GLOBECOM Workshops*, Miami, FL, USA, Dec. 2010, pp. 1799–1804.
- [6] E. Yanmaz, R. Kuschning, and C. Bettstetter, "Channel measurements over 802.11a-based uav-to-ground links," in *Proc. IEEE GLOBECOM Workshops*, Houston, TX, USA, Dec. 2011, pp. 1280–1284.
- [7] D. W. Matolak and R. Sun, "Air-ground channel characterization for unmanned aircraft systems: The over-freshwater setting," in *Proc. ICNS*, Herndon, VA, USA, Apr. 2014, pp. K1–1–K1–9.
- [8] M. Simunek, F. P. Fontán, P. Pecháč, and F. J. D. Otero, "Space diversity gain in urban area low elevation links for surveillance applications," *IEEE Trans. Antennas Propag.*, vol. 61, no. 12, pp. 6255–6260, Dec. 2013.
- [9] K. Takizawa, T. Kagawa, S. Lin, F. Ono, H. Tsuji, and R. Miura, "C-band aircraft-to-ground (a2g) radio channel measurement for unmanned aircraft systems," in *Proc. WPMC*, Sydney, Australia, Sept. 2014, pp. 754–758.
- [10] J. Zelený, F. Pérez-Fontán, and P. Pecháč, "Initial results from a measurement campaign for low elevation angle links in different environments," in *Proc. EuCAP*, Lisbon, Portugal, May 2015, pp. 1–4.
- [11] T. J. Willink, C. C. Squires, G. W. K. Colman, and M. T. Muccio, "Measurement and characterization of low-altitude air-to-ground mimo channels," *IEEE Trans. Veh. Technol.*, vol. 65, no. 4, pp. 2637–2648, Apr. 2016.
- [12] K. Daniel, M. Putzke, B. Dusza, and C. Wietfeld, "Three dimensional channel characterization for low altitude aerial vehicles," in *Proc. ISWCS*, York, United Kingdom, Sept. 2010, pp. 756–760.
- [13] Y. Wu, Z. Gao, C. Chen, L. Huang, H. P. Chiang, Y. M. Huang, and H. Sun, "Ray tracing based wireless channel modeling over the sea surface near diaoyu islands," in *Proc. CCITSA*, Ilan, Taiwan, Dec. 2015, pp. 124–128.
- [14] Z. Shi, P. Xia, Z. Gao, L. Huang, and C. Chen, "Modeling of wireless channel between uav and vessel using the fDTD method," in *Proc. WiCOM*, Beijing, China, Sept. 2014, pp. 100–104.
- [15] M. Simunek, F. P. Fontán, and P. Pecháč, "The uav low elevation propagation channel in urban areas: Statistical analysis and time-series generator," *IEEE Trans. Antennas Propag.*, vol. 61, no. 7, pp. 3850–3858, Jul. 2013.
- [16] N. Goddemeier and C. Wietfeld, "Investigation of air-to-air channel characteristics and a uav specific extension to the rice model," in *Proc. IEEE GLOBECOM Workshops*, San Diego, CA, USA, Dec. 2015, pp. 1–5.
- [17] D. W. Matolak and R. Sun, "Initial results for air-ground channel measurements & modeling for unmanned aircraft systems: Over-sea," in *Proc. IEEE Aerospace Conf.*, Big Sky, MT, USA, Mar. 2014, pp. 1–15.
- [18] R. Sun and D. W. Matolak, "Over-harbor channel modeling with directional ground station antennas for the air-ground channel," in *Proc. IEEE MILCOM*, Baltimore, MD, USA, Oct. 2014, pp. 382–387.
- [19] D. Matolak and R. Sun, "Air-ground channel characterization for unmanned aircraft systems-part i: Methods, measurements, and models for over-water settings," *IEEE Trans. Veh. Technol.*, vol. PP, no. 99, pp. 1–1, 2016.
- [20] R. Sun and D. Matolak, "Air-ground channel characterization for unmanned aircraft systems-part ii: Hilly & mountainous settings," *IEEE Trans. Veh. Technol.*, vol. PP, no. 99, pp. 1–1, 2016.
- [21] X. Cheng, C.-X. Wang, D. I. Laurenson, S. Salous, and A. V. Vasilakos, "An adaptive geometry-based stochastic model for non-isotropic mimo mobile-to-mobile channels," *IEEE Trans. Wireless Commun.*, vol. 8, no. 9, pp. 4824–4835, Sept. 2009.
- [22] Y. Yuan, C.-X. Wang, X. Cheng, B. Ai, and D. I. Laurenson, "Novel 3d geometry-based stochastic models for non-isotropic mimo vehicle-to-vehicle channels," *IEEE Trans. Wireless Commun.*, vol. 13, no. 1, pp. 298–309, Jan. 2014.
- [23] X. Cheng, C.-X. Wang, B. Ai, and H. Aggoune, "Envelope level crossing rate and average fade duration of nonisotropic vehicle-to-vehicle ricean fading channels," *IEEE Trans. on Intell. Transp. Syst.*, vol. 15, no. 1, pp. 62–72, 2014.
- [24] X. Cheng, Q. Yao, M. Wen, C.-X. Wang, L.-Y. Song, and B.-L. Jiao, "Wideband channel modeling and intercarrier interference cancellation for vehicle-to-vehicle communication systems," *IEEE J. on Sel. Area.Comm.*, vol. 31, no. 9, pp. 434–448, 2013.
- [25] L. Zeng, X. Cheng, C.-X. Wang, and X. Yin, "A 3D geometry-based stochastic channel model for UAV-MIMO channels," in *Proc. IEEE WCNC*, San Francisco, USA, Mar. 2017.
- [26] K. Jin, X. Cheng, X. Ge, and X. Yin, "Three Dimensional Modeling and Space-Time Correlation for UAV Channels," in *Proc. IEEE VTC-Spring*, Sydney, Australia, Jun., 2017.